ADVANCED MATERIALS
www.advmat.de

Blueprinting Photothermal Shape-Morphing of Liquid Crystal Elastomers

Alexa S. Kuenstler, Yuzhen Chen, Phuong Bui, Hyunki Kim, Antonio DeSimone, Lihua Jin,* and Ryan C. Hayward**

Liquid crystal elastomers (LCEs) are an attractive platform for dynamic shape-morphing due to their ability to rapidly undergo large deformations. While recent work has focused on patterning the director orientation field to achieve desired target shapes, this strategy cannot be generalized to material systems where high-resolution surface alignment is impractical. Instead of programming the local orientation of anisotropic deformation, an alternative strategy for prescribed shape-morphing by programming the magnitude of stretch ratio in a thin LCE sheet with constant director orientation is developed here. By spatially patterning the concentration of gold nanoparticles, uniform illumination leads to gradients in photothermal heat generation and therefore spatially nonuniform deformation profiles that drive out-of-plane buckling of planar films into predictable 3D shapes. Experimentally realized shapes are shown to agree closely with both finite element simulations and geometric predictions for systems with unidirectional variation in deformation magnitude. Finally, the possibility to achieve complex oscillatory motion driven by uniform illumination of a free-standing patterned sheet is demonstrated.

Morphing of 2D sheets into 3D shapes is a useful strategy to dynamically alter the physical properties of materials, offering diverse applications in fields ranging from biomedical devices to advanced manufacturing.[1] Over the past decade, numerous studies have focused on programming desired 3D structures of soft materials such as shape-memory polymers[2,3] and gels[4–7] by introducing spatial variations in thermal expansion/contraction, swelling, or molecular order.[8] A particularly useful class of materials to achieve dynamic 2D to 3D shape transformations are liquid crystal elastomers (LCEs), where the coupling between the orientational ordering of polymerized mesogens and the conformation of a polymer backbone can be leveraged for large, anisotropic deformations that are dictated by the director field.[9,10] Using oriented surface alignment layers[11] or microchannels,[12] director orientation can be patterned with a resolution approaching 10 µm.[13] A subsequent reduction of nematic ordering, usually driven by heating, leads to local contraction along the director and expansion along the transverse directions, driving out-of-plane buckling into 3D shapes that are "blueprinted" by the pattern of director orientation. However, while geometric methods allow for the deduction of the necessary in-plane director orientation field to generate a desired profile of Gaussian curvature,[14–17] there are a number of practical drawbacks to this approach. First, prescription of complex director fields requires significant processing, making high-throughput fabrication, and evaluation of designs challenging. Additionally, the surface alignment methods needed to specify director orientation with high spatial resolution are only amenable to certain chemistries due to the need for high mesogen content, and thus cannot be widely generalized to all LCE systems. For example, while classical LCE systems based on siloxanes,[18,19] as well as recently developed systems that rely on simple and efficient "click" chemistries,[20] offer attractive thermal and mechanical properties for shape-morphing systems, they typically only allow for alignment of the director field with coarse spatial resolution such as through application of shear stress[21–23] or magnetic fields.[24] To circumvent the need for a spatially varying director orientation, where the direction of deformation varies but the magnitude is constant, a potential alternative method to drive shape changes is to instead locally prescribe the magnitude of deformation within an otherwise homogeneous director field. While spatial variations in the extent of deformation have been widely employed for shape

A. S. Kuenstler, P. Bui, H. Kim, Prof. R. C. Hayward
Department of Polymer Science and Engineering
University of Massachusetts
Amherst, MA 01003, USA
E-mail: hayward@umass.edu
Y. Chen, Prof. L. Jin
Department of Mechanical and Aerospace Engineering
University of California, Los Angeles
Los Angeles, CA 90095, USA
E-mail: lihuajin@seas.ucla.edu
Prof. A. DeSimone
MathLab
SISSA-International School for Advanced Studies
Trieste 34136, Italy
E-mail: desimone@sissa.it
Prof. A. DeSimone
Department of Excellence in Robotics and AI
Scuola Superiore Sant'Anna
Pisa 56127, Italy
The ORCID identification number(s) for the author(s) of this article can be found under https://doi.org/10.1002/adma.202000609.

DOI: 10.1002/adma.202000609

programming of isotropic gels,[4,7,25–28] and briefly considered in seminal theoretical work on LC polymers,[29] this approach has yet to be experimentally realized in LCE systems. Furthermore, no theory for this means of shape programming in anisotropic materials exists despite the potential generality of this method to any LCE system that can be aligned into a monodomain with a unidirectional director field.

While most LCE systems rely on uniform heating to trigger shape change, optically driven shape-morphing is an attractive approach owing to the remote deployability, spatiotemporal control, and dynamic reconfigurability offered by using light as a control stimulus. Furthermore, light-responsive systems are particularly useful for programming deformation profiles, either through spatiotemporally patterned light fields or flood illumination of materials containing localized inclusions of photothermal or photochemical moieties.[8] Programmed buckling in response to both patterned and flood illumination has been widely exploited in gel[30–32] and shape-memory polymer systems.[33–36] In contrast, work on liquid crystalline materials has focused primarily on the use of spatially patterned light[37–40] with a few exceptions including azobenzene-containing LCEs with shapes blueprinted by director orientation[41] and glassy LC polymer cantilevers with coarsely patterned photothermal hinges.[42]

Recently, we introduced a method to spatially pattern gold nanoparticles (AuNPs) in LCE fibers[43] and hydrogel sheets[44] with high spatial resolution using UV-induced photoreduction of gold salt.[45,46] Following patterning, exposure to visible light induces localized photothermal deformation that drives shape-morphing. In this work, we explore the utility of this method to blueprint shape changes of thin LCE nanocomposite (LCENC) sheets with unidirectional in-plane director fields in response to flood illumination. Specifically, we show that discrete patterns of photothermal inclusions can generate a rich array of dynamic shape changes due to buckling driven by nearly discontinuous changes of in-plane deformation. Furthermore, smooth variations in deformation can be programmed via grayscale patterning of AuNP absorbance to yield more complex shape changes. Finite element method (FEM) simulations are used to help understand the shapes selected by these materials, in concert with an analytical model based on the principles of Gaussian morphing[4,47–49] that provides a general approach to the design of axisymmetric shapes through unidirectionally varying stretch profiles.

To fabricate monodomain LCEs, 50 μm thick planar nematic films are synthesized following the work of Ahn and co-workers (Scheme S1, Supporting Information).[50] This chemistry is employed due to its amenability to formation of monodomain samples with relatively low nematic-isotropic transition temperatures (T_{NI}) and large thermomechanical strains. Briefly, *n*-dodecylamine and 8-amino-1-octanol are mixed in a 1:1 molar ratio with the diacrylate mesogen RM82 with an overall stoichiometry of acrylate:amine functionalities of 1.1:1, selected to afford a cross-link density that allows for large strains while maintaining sufficient mechanical robustness. All reactants are melted in a vial with 1 wt% photoinitiator, filled between two rubbed polyimide-coated glass slides, and oligomerized in an oven overnight at 55 °C. Following oligomerization, films are photopolymerized under UV light and the resulting monodomain samples harvested. To impart photoresponsiveness, gold nanoparticles (AuNPs) are produced by in-situ photoreduction of gold salt within the preformed LCE films as previously reported.[43] LCE samples are swollen with a solution of $HAuCl_3$, oleylamine, and photoinitiator and exposed to UV light through a photomask to produce AuNPs via photochemical reduction (**Figure 1**A). Because the degree of gold reduction is controlled by the dose of UV light, the resulting absorbance of the nanocomposite can be spatially programmed using grayscale photomasks (Figure 1B).[26]

The as-synthesized films are monodomain with a constant director orientation (Figure S1, Supporting Information) with an order parameter of $S \approx 0.6$ as measured by wide-angle X-ray scattering (WAXS),[51] with a glass transition temperature of $T_g \approx -4$ °C, a broad $T_{NI} \approx 100$ °C, and an elastic modulus parallel to the director of $E \approx 9$ MPa (Figure S2, Supporting Information). We note that introduction of AuNPs does not significantly affect the thermal or mechanical properties of the films, as evidenced by calorimetry, thermogravimetry, and tensile tests (Figure S2, Supporting Information). Upon uniformly heating above 40 °C, samples reversibly contract along the director and expand in the perpendicular directions, ultimately contracting to 60% of their initial length along the director when heated to 120 °C (Figure 1C). To probe the effect of photothermal heat generation on deformation, films are placed on a hot plate at a defined temperature and exposed to 200 mW cm^{-2} of light with wavelength 530 nm. The length at each temperature is recorded to define a stretch ratio, $\lambda = l_{final}/l_{initial}$ where $l_{initial}$ is defined as the length along the director at room temperature. As shown in Figure 1C for the case of maximum light absorbance, a photoinduced temperature change of $\Delta T \approx 20$ °C (Figure S3, Supporting Information) is observed. We note that in principle, this temperature change could be substantially greater and is limited by the intensity of the incident light source. Photodeformation is maximized when samples are held at 80–90 °C due to the proximity to T_{NI}; thus, all subsequent experiments are conducted at an ambient temperature of 85 °C. Because AuNP absorbance determines the magnitude of temperature change upon photothermal heating, control of light dose during photoreduction can be used to systematically program the resulting photodeformation. As shown in Figure 1D, the stretch λ due to photothermal heating can be programmed from 0.77 to 0.92 by controlling the transparency of the photomask to UV light from 0% black (nearly transparent to UV light) and 100% black (nearly opaque) during patterning. This introduces the possibility to locally control photodeformation—and thus shape transformation—through judicious design of photomasks.

To connect the patterned photothermal heat generation to shape transformation, we develop FEM simulations and a geometric model. In the FEM simulations, LCE sheets are modeled using the neo-classical free energy density[52,53] implemented into Abaqus as a user subroutine UMAT. A stretch–temperature relation, fit to the experimental measurement (Figure 1C), is introduced into the free energy to describe the temperature-dependent anisotropy of LCEs (see Experimental Section; Supporting Information). Once a temperature field corresponding to a specific design of photothermal patterning is prescribed, the equilibrium shape is solved by FEM in Abaqus.

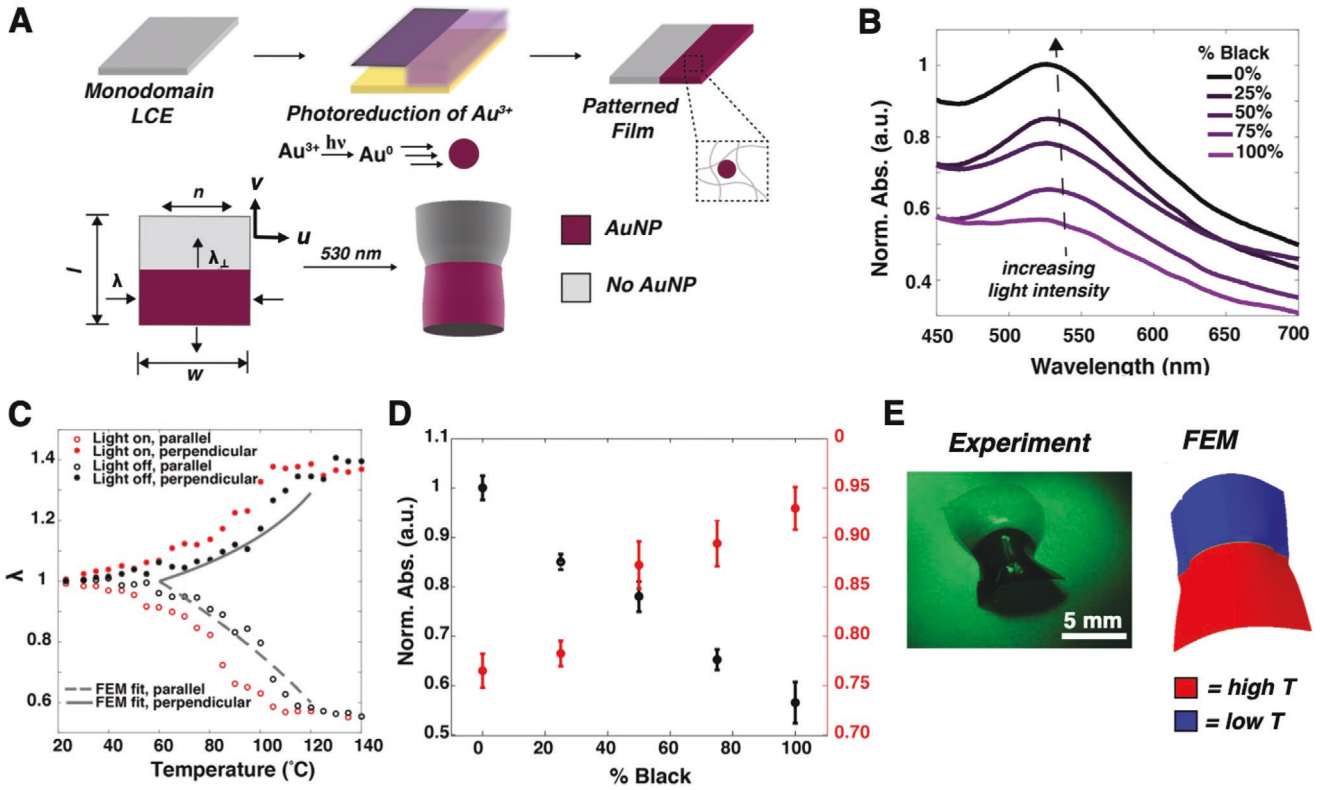

Figure 1. Photopatterning and photothermal properties of LCENCs. A) AuNPs are spatially incorporated into LCEs via photoreduction of gold salt with UV light. Upon illumination with visible light, local heating induces a contraction along the director and buckling into a prescribed shape. B) AuNP absorbance is controlled by modulating the light dose via grayscale photomasks that vary from 0% black (transparent) to 100% black (opaque). C) Stretch versus temperature with (red) and without (black) photothermal heating for the case of highest absorbance. Because of the high T_{NI} of these materials experiments are performed at 85 °C to maximize photodeformation. D) Absorbance and stretch as functions of the opacity of the photomasks. Stretch can be spatially programmed over a range of 20%. E) Example of a sheet programmed with a bistrip geometry. Contraction along the director parallel to the interface between photothermally heated and non-heated regions results in rolling about an axis perpendicular to this interface.

To model these shape changes geometrically, we turn to the principle of Gaussian morphing,[48,49] previously exploited for isotropic systems, and apply it to the anisotropic case considered here. In this model, the in-plane deformation due to photothermal heat generation defines a "target metric" that describes how the distance between points in the flat sheet should change upon deployment to generate a shape of defined curvature. We consider the case of sheets with uniform orientation of the director along the u-axis (Figure 1A), where the magnitude of stretch λ is constant along u and varies as a function of v. Thus, the metric tensor is given by

$$g = \begin{bmatrix} \lambda^2(v) & 0 \\ 0 & \dfrac{1}{\lambda(v)} \end{bmatrix} \tag{1}$$

Crucially, in this case, the local magnitude of stretch varies while the direction is constant, similar to the case of isotropic gels[4,7,25–28] and equibiaxially strained thermoplastics[35,54] but distinct from the case of a director field with patterned orientation but uniform magnitude of stretch.[11,17] Using Gauss's *theorema egregium* (see Supporting Information for a more detailed discussion), the Gaussian curvature can be calculated from the metric tensor by

$$K = -\frac{1}{\sqrt{\lambda}}\left(\sqrt{\lambda}\lambda'\right)' = -\frac{2}{3\sqrt{\lambda}}\left(\lambda^{3/2}\right)'' \tag{2}$$

Thus, by solving Equation (2) for a desired curvature profile $K(v)$, a corresponding stretch profile $\lambda(v)$ can be computed. Finally, using an experimentally determined calibration curve of stretch versus grayscale, a photomask can be generated to pattern the necessary photothermal profile into the nematic sheets (see Supporting Information for additional detail).

Using this method, we first investigate the effect of discretely patterned deformation profiles on the buckling of nematic sheets using a bistrip geometry, where one-half of a square sheet is patterned with a stripe of AuNPs such that the photoactive region bisects the length of the sheet with the long axis of the stripe parallel to the director (Figure 1A). For the case where the lateral dimensions of the square film are much greater than the thickness (here, width/thickness = 200), heat dissipation by convection limits thermal broadening across the interface between the photoactive and non-photoactive

regions (Figure S3B, Supporting Information). In addition, despite a through-thickness gradient in heat generation due to the strong absorption of light by the nanoparticles that is necessary to generate appreciable temperature changes, the thin nature of these films ensures that the resulting temperature distribution is nearly constant through the thickness of the film (Figure S3C, Supporting Information). For the simple case of a discrete photothermally heated stripe, the equilibrium in-plane length is almost discontinuous across the stripe interface as the photoactive region contracts along the director and the energetic cost of this step-change in deformation is relieved by buckling out-of-plane. For square films with side length $l = 10$ mm, the films preferentially roll about an axis perpendicular to the photothermal interface to form a bottleneck shape upon illumination as shown in Figure 1E, where the non-heated and heated regions adopt different radii of curvature that are smoothly connected over the interfacial region as predicted by FEM. We note that films tend to roll with the direction of curvature away from the light. This suggests that while small asymmetries in heating through the thickness inevitably exist due to the decay in light intensity, this is not the dominant factor in biasing the buckling direction of the film, since a higher temperature at the surface of the film facing the incident light should prefer curvature toward the light source. This shape transformation is analogous to the case of isotropic hydrogel bistrips with two discrete regions of cross-link density.[55] This shape transformation can be rationalized as follows: while a discontinuous target metric encodes divergent positive and negative Gaussian curvature on either side of the interface, the non-zero thickness of a real sheet, and the corresponding bending energy cost to deform it, causes the curvature to be smoothed out across the interface into regions of finite Gaussian curvature with opposite signs. The resulting shape consists of two zero-K regions on either end of the sheet, smoothly connected by a neck that contains regions of both positive and negative Gaussian curvature, wherein stretching energy (i.e., deviations from the discontinuous target metric) balances the overall bending energy of the sheet.

To probe the utility of this method to program a wider variety of shapes, a series of additional patterns are investigated. For example, illumination of a square sheet with a centered rectangular inclusion with the long axis oriented parallel to the director results in a saddle-like shape that is symmetric about the axes parallel and perpendicular to the director that bisect the center of the film (**Figure 2**A). Placement of a photothermal region in one quadrant of the film drives bending about an axis diagonally bisecting the sheet, resulting in a wrinkled hyperbolic surface (Figure 2B). Finally, inclusion of a large square in the center of the sheet drives rolling about an axis perpendicular to the director and wrinkling along the edges of the sheet

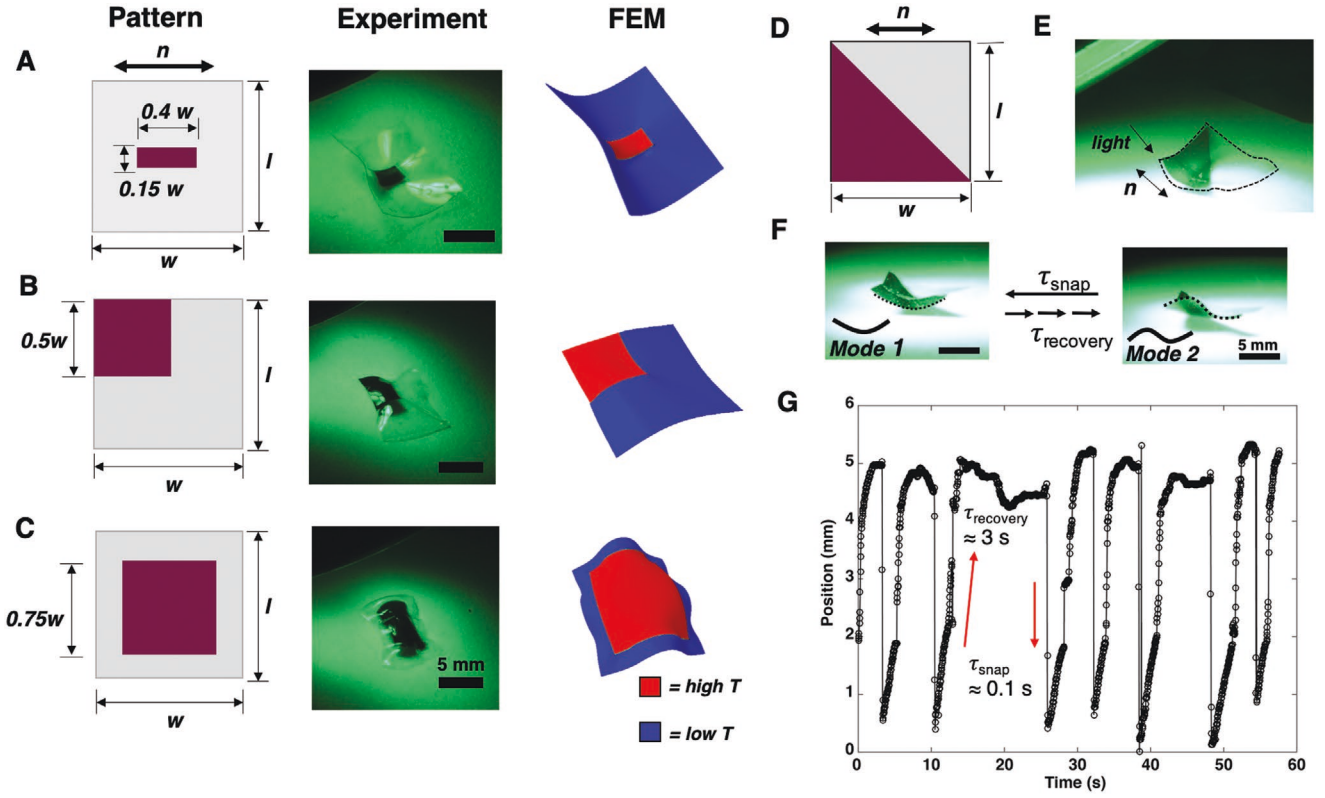

Figure 2. Shape transformation via localized photothermal inclusions. Buckling into different shapes in response to A) rectangular and B,C) square inclusion is demonstrated experimentally and the resulting shapes are predicted via FEM. D,E) A square film is patterned with the photothermal region bisecting the film at 45° with respect to the director with incident light on the corner of the photothermal region. F) The film snaps from a half wavelength to a full wavelength wrinkle reversibly. Upon relaxing to the initial state, the process repeats. G) Position of the edge of the film with respect to the substrate versus time. The film gradually evolves over a few seconds to Mode 2 before snapping through to Mode 1 in ≈0.1 s. The film exhibits mechanical bistability between the two modes and autonomously oscillates between them for the duration of illumination.

(Figure 2C). These deformations are similar to those observed in nematic sheets with polydomain inclusions[56] and isotropic gels with local photothermal inclusions[44] and again result from a balance of stretching and bending energies as the films attempt to accommodate the discontinuous target metric.

Remarkably, a simple change in the direction of the film edges with respect to the director and photothermal inclusions leads to more complex behavior. When nanoparticles are patterned in half of the film with the interface between the photoactive and non-photoactive region extending diagonally between opposing corners of a square film at a 45° angle to the director (Figure 2D), flood illumination from directly above the film drives wrinkling as observed for the other striped case (Figure S4, Supporting Information). However, when the sheet is illuminated from a 30° angle with respect to the substrate along the edge parallel to the director, the film is observed to oscillate continuously between two buckling modes (Figure 2E–G; Videos S1, S2, Supporting Information). Initially, the film adopts a geometry such that the edge of the film along the director curls about an axis perpendicular to the director, denoted as Mode 1. However, the shape slowly evolves over a few seconds to become a full wavelength wrinkle (Mode 2) that quickly snaps back to Mode 1 after several seconds as evidenced by the nearly discontinuous change in film edge displacement when tracked from a 60 fps video (Figure 2F), with a characteristic snapping time of ≈0.1 s. This cycle then repeats for the duration of illumination. Intersnap times range from 1.2 to 11.8 seconds, with an average time of 3.8 seconds. While oscillation due to self-shadowing effects[37,42,57–59] and snapping between two bistable shapes[60,61] has been reported previously in nematic beams, cyclic oscillation via photoinduced snapping has only been reported in one other case,[62] to our knowledge. We hypothesize that this phenomenon is driven by self-shadowing, where slight changes in the incident light intensity due to deformation toggles the equilibrium between buckling modes. Though our FEM methods are unable to capture dynamic behavior at this time, we find that if a strain profile is imposed that is consistent with a high light intensity on the edge of the film and with less stretch in areas where the light would be blocked during shape evolution, Mode 2 is predicted, suggesting that self-shadowing is capable of driving a transition in buckled geometry, and hence the oscillatory snapping behavior observed here (See Figure S5, Supporting Information, for more details). Films of other geometries do not demonstrate oscillatory behavior when exposed to similar oblique illumination conditions (Figure S6, Supporting Information). While further study is warranted to fully understand the underlying mechanics of this phenomenon, this behavior suggests that localized deformation can be leveraged for non-equilibrium behavior and impulsive motion upon judicious design of photoinduced buckling instabilities and illumination conditions.

Next, we explore the utility of smoothly varying spatial gradients in absorption to introduce continuous in-plane stretch profiles into nematic sheets, which provides opportunities to program shapes with arbitrary Gaussian curvatures. As a proof-of-concept, we first investigate the "forward" problem, that is, defining a stretch profile and evaluating the match between experiments, FEM simulations, and geometric predictions for the resulting 3D shape. As a convenient test case, we use stretch profiles of the following form to program square sheets:

$$\lambda(\xi) = \lambda_{\min} + (\lambda_{\max} - \lambda_{\min}) \exp\left(-\frac{1}{2}\left(\frac{2\xi - 1}{d}\right)^2\right) \tag{3}$$

where $\xi = \frac{\nu}{w} \in [0,1]$, $\lambda_{\min}$ and $\lambda_{\max}$ are the minimum and maximum experimentally accessible stretches, respectively, and d is a dimensionless parameter that controls the spatial extent of variations in λ (**Figure 3**A). Indeed, as predicted by Equation (2), as d is reduced, the resulting curvature increases in magnitude and becomes concentrated in a smaller region. Using the corresponding metric tensor, given by Equation (1), theory and FEM (Figure 3B–D) predict buckling into candy wrapper-like shapes, with a ridge of positive Gaussian curvature in the middle of the sheet that smoothly progresses along ν to valley regions of negative Gaussian curvature that evolve to zero Gaussian curvature at the edges. To investigate these shape transformations experimentally, samples are patterned using photomasks generated in Matlab from a calibration curve of stretch versus percent black (see Supporting Information for photomasks and additional details). Experimental results (Figure 3E; Figure S7, Supporting Information) match the predicted deformations, with greater curvature and a tighter characteristic radius of curvature of the ridge as d decreases. We find that the Gaussian curvatures observed by FEM (Figure 3B) are in very good agreement with the ones predicted by Equation (2), and furthermore that the realized 3D shapes correspond closely to those from geometric predictions (Figure 3C; Supporting Information). This striking agreement demonstrates the robustness of the shape-morphing concept developed here and suggests its potential for generalization to other chemistries and materials.

To truly program shape transformation, the inverse problem—that is, computing the stretch profile $\lambda(\nu)$ that leads to a desired 3D shape upon actuation—needs to be solved. While the corresponding differential geometry has been developed for isotropic gels with differential swelling[4,5,47] and nematic sheets with varying director orientation,[14,17] we are not aware of previous solutions for the anisotropic case of varying stretch magnitude with a homogenous director orientation. As a first step, we focus here on shapes with constant negative and positive Gaussian curvature, with the appropriate stretch functions obtained by numerically solving Equation (2) within the constraint of the stretches achievable in our system and constructing a polynomial fit to the solution (see Figure S8, Supporting Information, for details). The target negative and positive curvature, calculated stretch profiles, and simulated curvature generated by FEM are shown in **Figure 4**A,D. The calculated stretch profiles prescribe high deformation in the center of the sheet and low deformation at the edges parallel to the director field in the case of constant negative Gaussian curvature and the opposite—low deformation in the middle and high deformation at the edges—for the case of constant positive Gaussian curvature. The simulated curvatures from FEM match the target constant curvatures quite well in the center portions of the films but deviate at the edges, presumably reflecting an elastic "boundary layer"[63] that lowers the bending energy for a non-zero thickness sheet. The corresponding samples are prepared using photomasks generated from the

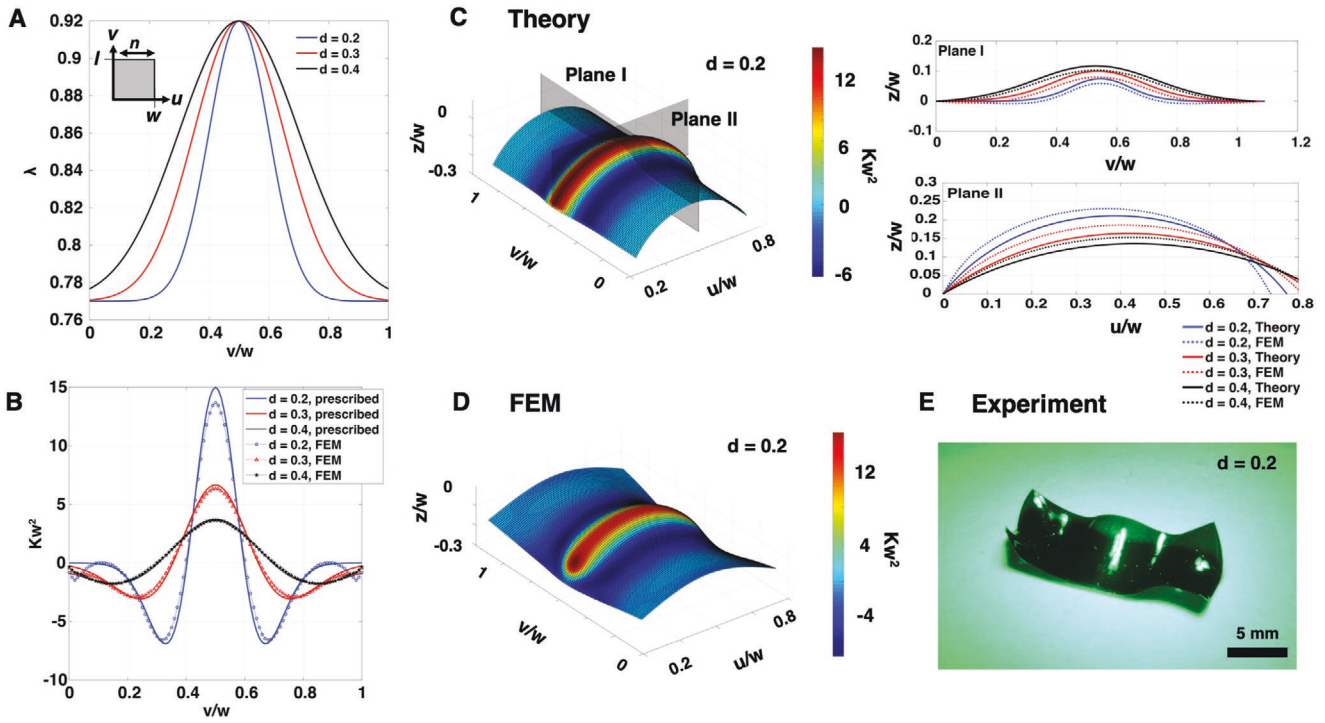

Figure 3. Patterning smoothly curved sheets with Gaussian stretch profiles. A) Stretch profiles λ for different values of d for $w = l$ (inset). B) Prescribed and FEM Gaussian curvature as a function of v at $u/w = 0.5$. C) Shape prediction of $d = 0.2$ by theory (left) and comparison of theory to FEM simulations (right) for different values of d. D) Shape prediction of $d = 0.2$ by FEM. E) Experimental result for $d = 0.2$ demonstrates buckling into a candy wrapper-like shape due to regions of highly localized Gaussian curvature that closely matches the predicted shape by theory and FEM. Results for $d = 0.3$ and 0.4 are provided in the Supporting Information.

calculated stretch profiles (see Supporting Information) and experiments show buckling of LCE sheets into a saddle-like shape and a shallow spherical cap-like shape for negative and positive Gaussian curvature, respectively, matching the predictions of the accompanying FEM simulations and geometric models (Figure 4B,C,E,F; Figure S9, Supporting Information). Interestingly, FEM predicts that a non-axisymmetric saddle shape should be lower energy than the observed axisymmetric shape in the case of constant negative Gaussian curvature (Figure S10, Supporting Information). However, the non-axisymmetric shape is not observed experimentally, possibly due to imperfections in sample fabrication or kinetic selection of the axisymmetric shape. We note that the observed shapes are analogous to those experimentally realized in LCEs with patterned axisymmetric director fields about a +1 defect.[16]

In summary, we have demonstrated a method combining experiments, FEM simulations, and geometric predictions to program photoactive shape-morphing from monodomain LCE sheets with a unidirectional director by spatially controlling photothermal heat generation. Discontinuous metrics introduced via localized photothermal inclusions are shown to drive buckling into both static shapes and autonomously oscillating forms. Furthermore, we developed a new theory based on Gaussian morphing to encode smoothly varying stretch profiles to rationally approach the design of targeted shapes. We anticipate that this fabrication method is generalizable to a variety of chemistries that are incompatible with methods to spatially pattern in-plane director fields, opening up new opportunities for shape-morphing in a variety of liquid crystalline polymer materials.

Experimental Section

Materials: 1,4-Bis[4-(6-acryloyloxyhexyloxy)benzoyloxy]-2-methylbenzene (RM82) was purchased from Synthon Chemicals and used as received. 8-amino-1-octanol and *n*-dodecylamine were purchased from Tokyo Chemical Industries. 2,2-dimethoxy-2-phenyl-acetophenone (Irgacure 651), oleylamine, and gold(III) chloride trihydrate ($HAuCl_4$) were purchased from Sigma Aldrich.

LCE Fabrication: The procedure of Ahn and co-workers[50] was followed with slight modification. RM82, dodecylamine, and 8-amino-1-octanol were combined in a molar ratio of 1.1:0.5:0.5 with 2.5 wt% of Irgacure 651 in a vial and melted at ≈85 °C and vortexed repeatedly. Following evacuation to remove air bubbles, the molten mixture was infiltrated via capillary action into alignment cells composed of two glass slides coated with Elvamide polyimide (DuPont), rubbed with a velvet cloth, and set to 50 µm thickness with glass spacers. Samples were placed in an oven at 55 °C to oligomerize overnight, subsequently cured with UV light (10 mW cm^{-2}) for 30 min and harvested by soaking in warm water and gently opening the alignment cells with a razor blade.

Photopatterning of Nanocomposites: Stock solutions of $HAuCl_4$ (11.8 mg, 0.035 mmol) in acetone (0.3 mL), oleylamine (59 mg, 0.22 mmol) in toluene (0.5 mL), and Irgacure 651 (56.2 mg, 0.22 mmol) in toluene (0.5 mL) were freshly prepared. To prepare the gold nanoparticle precursor solution, 200 µL of $HAuCl_4$, 400 µL of Irgacure 651, and 200 µL of oleylamine stock solutions were sequentially added to a vial and diluted with 800 µL of toluene. Films were swelled in gold solution, blotted on filter paper to remove excess solution, and

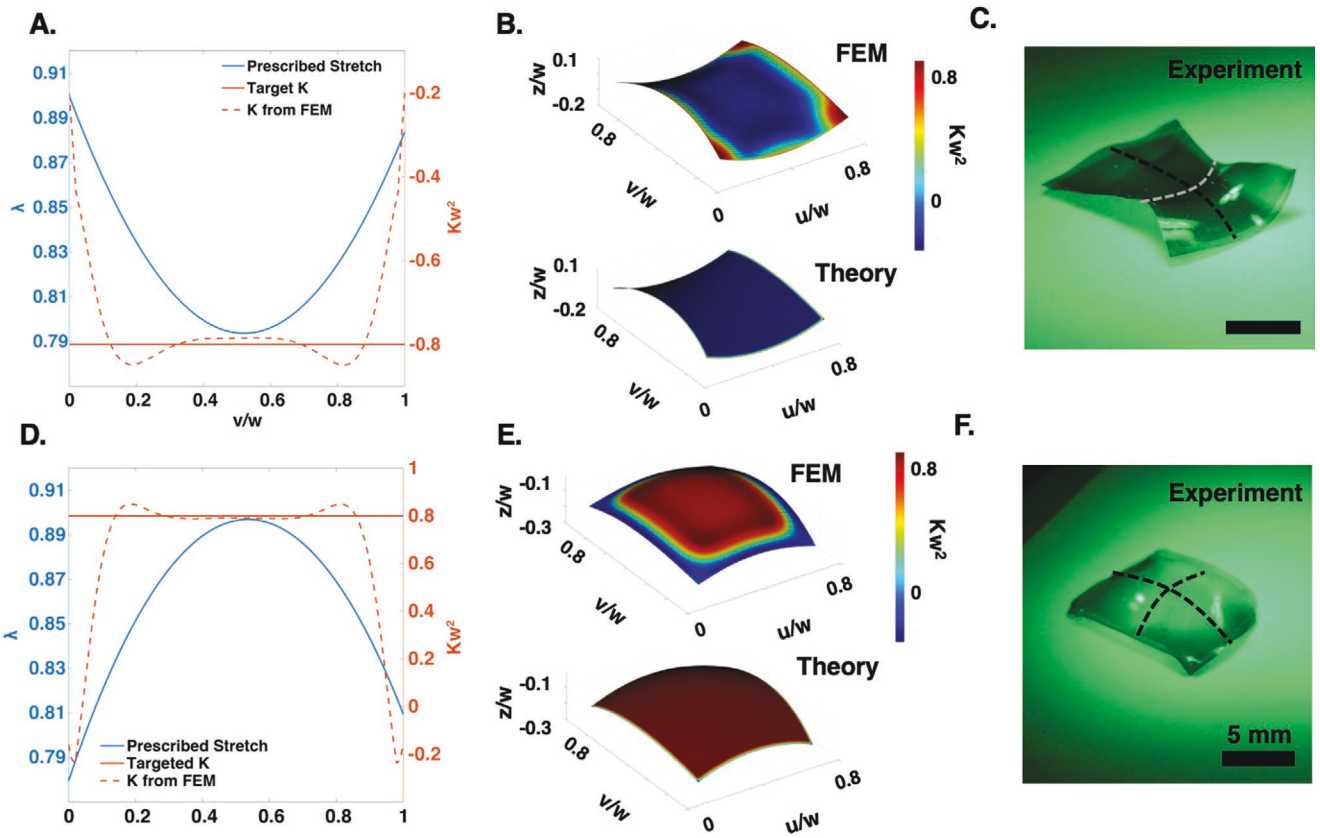

Figure 4. Programmed constant negative and positive Gaussian curvature via ninth-order polynomial stretch profiles. A) Prescribed and predicted Gaussian curvature, B) FEM simulation (top) and theory (bottom) and C) experiment for negative Gaussian curvature. D) Prescribed and predicted Gaussian curvature, E) FEM simulation, and F) experiment for positive Gaussian curvature. White and black lines are drawn as guides to the eyes, with black and white denoting positive and negative curvatures, respectively.

sandwiched between a glass slide and a photomask. Photomasks were prepared in Matlab and Adobe Illustrator, fabricated via inkjet printing (HP LaserJet 500) on plastic transparency films (Apollo Laser Printer Transparency Film), and glued on glass coverslips. Samples were exposed to 30 mW cm^{-2} of light with 365 nm wavelength (Thorlabs) for 10 s, developed in acetone for 60 min to remove unreacted gold salt, and dried.

Instruments and Measurement: Ultraviolet-visible absorption spectra were recorded on a fiber optic spectrometer (Ocean Optics Flame). To evaluate photoactuation, samples were placed on a hot plate covered with filter paper to prevent sticking and heated to 85 °C. All actuation experiments were performed with a 530 nm light emitted diode (LEDSupply) generating an intensity of 200 mW cm^{-2} and shape transformations were recorded using a camera (Nikon 5500). Displacement data during oscillation was extracted from recorded videos recorded at 60 fps using Tracker software (Open Source Physics). Because the time-scale of snapping is similar to that of the frame rate, blurring of images prevented the use of some frames for tracking analysis during snapping.

FEM Simulations: In the finite element simulations, thin LCE sheets are modeled with the same geometry as that in the experiments, that is, a square shape with a width-to-thickness ratio of 200. The LCE sheets were modeled using the neo-classical free energy density[52,53] implemented into Abaqus as a user subroutine UMAT (see Supporting Information for details). The ratio of the bulk modulus to the shear modulus K/μ is set as 500, which indicates that the Poisson's ratio is 0.499 and thus the sheets are nearly incompressible. A stretch–temperature relation (Figure 1C), fitted to the experimental measurement, is introduced into the free energy to describe the temperature-dependent anisotropy of LCEs (Supporting Information).

$$\lambda = 0.6\sqrt{1+1.778\frac{120-T}{60}},\ 60\ ^{\circ}\mathrm{C} \le T \le 120\ ^{\circ}\mathrm{C} \tag{4}$$

Although in experiments the stretch is defined with respect to the length at room temperature, in FEM simulations the lengths below 60 °C and above 120 °C are treated as those at 60 °C and 120 °C, respectively, because the difference is negligible. The above stretch–temperature relation indicates that the nematic LCEs start to deform at 60 °C and continuously deform until 120 °C, yielding a maximum stretch of 0.6 parallel to the director. Using the above equation, the stretch patterns in the experiments are converted into temperature distributions, which are assigned to the LCE sheets as predefined fields. The element type is 3D hybrid quadratic brick with reduced integration (Abaqus type C3D20RH). A mesh refinement study was performed to ensure that there are at least three elements along the thickness and that the aspect ratio of a single element is no greater than 5. As a result, approximately 3×10^4 elements are involved in each finite element model. The LCE sheets in all the simulations have free boundary conditions, except the case shown in Figure 4B, in which symmetric boundary conditions about $u/w = 0.5$ is applied. Artificial damping is introduced into the static general procedure such that the sheets can snap to a stable equilibrium state when loss of stability occurs. The damping factor in the simulations is determined based on the dissipated energy fraction, which is set as 1×10^{-5}, a value that can suppress instabilities without having a significant effect on the solutions.

Supporting Information

Supporting Information is available from the Wiley Online Library or from the author.

Acknowledgements

A.S.K. and Y.C. contributed equally to this work. Support for this work was provided by the Office of Naval Research through the MURI on Photomechanical Materials (ONR N00014-18-1-2624), National Science Foundation through Grant No. CMMI 1925790, and European Research Council through Advanced Grant 340685-MicroMotility. The authors thank Daria Atkinson for helpful discussions.

Conflict of Interest

The authors declare no conflict of interest.

Keywords

liquid crystal elastomers, photoresponsive materials, shape programming

Received: January 27, 2020
Revised: March 2, 2020
Published online: March 16, 2020

[1] Y. Liu, J. Genzer, M. D. Dickey, *Prog. Polym. Sci.* **2016**, *52*, 79.
[2] Q. Zhao, H. J. Qi, T. Xie, *Prog. Polym. Sci.* **2015**, *49–50*, 79.
[3] A. Lendlein, O. E. C. Gould, *Nat. Rev. Mater.* **2019**, *4*, 116.
[4] Y. Klein, E. Efrati, E. Sharon, *Science* **2007**, *315*, 1116.
[5] J. Kim, J. a. Hanna, M. Byun, C. D. Santangelo, R. C. Hayward, *Science* **2012**, *335*, 1201.
[6] A. S. Gladman, E. A. Matsumoto, R. G. Nuzzo, L. Mahadevan, J. A. Lewis, *Nat. Mater.* **2016**, *15*, 413.
[7] S. J. Jeon, A. W. Hauser, R. C. Hayward, *Acc. Chem. Res.* **2017**, *50*, 161.
[8] A. S. Kuenstler, R. C. Hayward, *Curr. Opin. Colloid Interface Sci.* **2019**, *40*, 70.
[9] T. J. White, D. J. Broer, *Nat. Mater.* **2015**, *14*, 1087.
[10] R. S. Kularatne, H. Kim, J. M. Boothby, T. H. Ware, *J. Polym. Sci., Part B: Polym. Phys.* **2017**, *55*, 395.
[11] T. H. Ware, M. E. McConney, J. J. Wie, V. P. Tondiglia, T. J. White, *Science* **2015**, *347*, 982.
[12] Y. Xia, G. Cedillo-Servin, R. D. Kamien, S. Yang, *Adv. Mater.* **2016**, *28*, 9637.
[13] B. A. Kowalski, V. P. Tondiglia, T. Guin, T. J. White, *Soft Matter* **2017**, *13*, 4335.
[14] H. Aharoni, E. Sharon, R. Kupferman, *Phys. Rev. Lett.* **2014**, *113*, 257801.
[15] P. Plucinsky, B. A. Kowalski, T. J. White, K. Bhattacharya, *Soft Matter* **2018**, *14*, 3127.
[16] B. A. Kowalski, C. Mostajeran, N. P. Godman, M. Warner, T. J. White, *Phys. Rev. E* **2018**, *97*, 012504.
[17] H. Aharoni, Y. Xia, X. Zhang, R. D. Kamien, S. Yang, *Proc. Natl. Acad. Sci. U. S. A.* **2018**, *115*, 7206.
[18] J. Küpfer, J. Küpfer, H. Finkelmann, H. Finkelmann, *Die Makromol. Chem.* **1991**, *12*, 717.
[19] H. Wermter, H. Finkelmann, *e-Polymers* **2001**, *1*, 111.
[20] M. O. Saed, A. H. Torbati, C. A. Starr, R. Visvanathan, N. A. Clark, C. M. Yakacki, *J. Polym. Sci., Part B: Polym. Phys.* **2017**, *55*, 157.
[21] C. M. Yakacki, M. Saed, D. P. Nair, T. Gong, S. M. Reed, C. N. Bowman, *RSC Adv.* **2015**, *5*, 18997.
[22] A. Kotikian, R. L. Truby, J. W. Boley, T. J. White, J. A. Lewis, *Adv. Mater.* **2018**, *30*, 1706164.
[23] M. O. Saed, C. P. Ambulo, H. Kim, R. De, V. Raval, K. Searles, D. A. Siddiqui, J. M. O. Cue, M. C. Stefan, M. R. Shankar, T. H. Ware, *Adv. Funct. Mater.* **2019**, *29*, 1806412.
[24] Y. Yao, J. T. Waters, A. V. Shneidman, J. Cui, X. Wang, N. K. Mandsberg, S. Li, A. C. Balazs, J. Aizenberg, *Proc. Natl. Acad. Sci. U. S. A.* **2018**, *115*, 12950.
[25] Z. L. Wu, M. Moshe, J. Greener, H. Therien-Aubin, Z. Nie, E. Sharon, E. Kumacheva, *Nat. Commun.* **2013**, *4*, 1586.
[26] J. H. Na, N. P. Bende, J. Bae, C. D. Santangelo, R. C. Hayward, *Soft Matter* **2016**, *12*, 4985.
[27] H. Thérien-Aubin, M. Moshe, E. Sharon, E. Kumacheva, *Soft Matter* **2015**, *11*, 4600.
[28] L. Huang, R. Jiang, J. Wu, J. Song, H. Bai, B. Li, Q. Zhao, T. Xie, *Adv. Mater.* **2017**, *29*, 1605390.
[29] C. D. Modes, K. Bhattacharya, M. Warner, *Proc. R. Soc. A* **2011**, *467*, 1121.
[30] Z. Zhu, E. Senses, P. Akcora, S. A. Sukhishvili, *ACS Nano* **2012**, *6*, 3152.
[31] E. Wang, M. S. Desai, S. W. Lee, *Nano Lett.* **2013**, *13*, 2826.
[32] A. W. Hauser, A. A. Evans, J. H. Na, R. C. Hayward, *Angew. Chem., Int. Ed.* **2015**, *54*, 5434.
[33] Y. Liu, J. K. Boyles, J. Genzer, M. D. Dickey, *Soft Matter* **2012**, *8*, 1764.
[34] Y. Liu, B. Shaw, M. D. Dickey, J. Genzer, *Sci. Adv.* **2017**, *3*, e1602417.
[35] A. M. Hubbard, R. W. Mailen, M. A. Zikry, M. D. Dickey, J. Genzer, *Soft Matter* **2017**, *13*, 2299.
[36] T. F. Scott, A. D. Schneider, W. D. Cook, C. N. Bowman, *Science* **2005**, *308*, 1615.
[37] A. W. Hauser, D. Liu, K. C. Bryson, R. C. Hayward, D. J. Broer, *Macromolecules* **2016**, *49*, 1575.
[38] M. Lahikainen, H. Zeng, A. Priimagi, *Nat. Commun.* **2018**, *9*, 4148.
[39] J.-A. Lv, Y. Liu, J. Wei, E. Chen, L. Qin, Y. Yu, *Nature* **2016**, *537*, 179.
[40] M. K. McBride, M. Hendrikx, D. Liu, B. T. Worrell, D. J. Broer, C. N. Bowman, *Adv. Mater.* **2017**, *29*, 1606509.
[41] S. K. Ahn, T. H. Ware, K. M. Lee, V. P. Tondiglia, T. J. White, *Adv. Funct. Mater.* **2016**, *26*, 5819.
[42] A. H. Gelebart, G. Vantomme, E. W. Meijer, D. J. Broer, *Adv. Mater.* **2017**, *29*, 1606712.
[43] A. S. Kuenstler, H. Kim, R. C. Hayward, *Adv. Mater.* **2019**, *31*, 1901216.
[44] H. Kim, J. Kang, Y. Zhou, A. S. Kuenstler, Y. Kim, C. Chen, T. Emrick, R. C. Hayward, *Adv. Mater.* **2019**, *31*, 1900932.
[45] M. L. Marin, K. L. Mcgilvray, J. C. Scaiano, *J. Am. Chem. Soc.* **2008**, *130*, 16572.
[46] A. S. Korchev, M. J. Bozack, B. L. Slaten, G. Mills, *J. Am. Chem. Soc.* **2004**, *126*, 10.
[47] E. Sharon, E. Efrati, *Soft Matter* **2010**, *6*, 5693.
[48] M. Arroyo, A. Desimone, *J. Mech. Phys. Solids* **2014**, *62*, 99.
[49] G. Cicconofri, M. Arroyo, G. Noselli, A. DeSimone, *Int. J. Nonlinear Mech.* **2020**, *118*, 103278.
[50] H. H. Yoon, D. Y. Kim, K. U. Jeong, S. K. Ahn, *Macromolecules* **2018**, *51*, 1141.
[51] M. Deutsch, *Phys. Rev. A* **1991**, *44*, 8264.
[52] L. Jin, Z. Zeng, Y. Huo, *J. Mech. Phys. Solids* **2010**, *58*, 1907.
[53] P. Bladon, M. Terentjev, M. Warner, *Phys. Rev. E* **1993**, *47*, R3838.
[54] R. W. Mailen, C. H. Wagner, R. S. Bang, M. Zikry, M. D. Dickey, J. Genzer, *Smart Mater. Struct.* **2019**, *28*, 045011.
[55] J. Kim, J. A. Hanna, R. C. Hayward, C. D. Santangelo, *Soft Matter* **2012**, *8*, 2375.
[56] C. Ahn, X. Liang, S. Cai, *Extreme Mech. Lett.* **2015**, *5*, 30.

[57] T. J. White, N. V. Tabiryan, S. V. Serak, U. A. Hrozhyk, V. P. Tondiglia, H. Koerner, R. A. Vaia, T. J. Bunning, *Soft Matter* **2008**, *4*, 1796.
[58] K. M. Lee, M. L. Smith, H. Koerner, N. Tabiryan, R. A. Vaia, T. J. Bunning, T. J. White, *Adv. Funct. Mater.* **2011**, *21*, 2913.
[59] A. H. Gelebart, D. J. Mulder, M. Varga, A. Konya, G. Vantomme, E. W. Meijer, R. L. B. Selinger, D. J. Broer, *Nature* **2017**, *546*, 632.
[60] M. R. Shankar, M. L. Smith, V. P. Tondiglia, K. M. Lee, M. E. McConney, D. H. Wang, L. S. Tan, T. J. White, *Proc. Natl. Acad. Sci. U. S. A.* **2013**, *110*, 18792.
[61] A. A. Skandani, S. Chatterjee, M. L. Smith, J. Baranski, D. H. Wang, L. S. Tan, T. J. White, M. R. Shankar, *Extreme Mech. Lett.* **2016**, *9*, 45.
[62] H. Zeng, M. Lahikainen, L. Liu, Z. Ahmed, O. M. Wani, M. Wang, H. Yang, A. Priimagi, *Nat. Commun.* **2019**, *10*, 5057.
[63] E. Efrati, E. Sharon, R. Kupferman, *Phys. Rev. E* **2009**, *80*, 016602.